Steady flow dynamics during granular impact

Abram H. Clark,[1,2] Lou Kondic,[3] and Robert P. Behringer[1]

[1]*Department of Physics & Center for Nonlinear and Complex Systems, Duke University, Durham, North Carolina 27708, USA*
[2]*Department of Mechanical Engineering and Materials Science, Yale University, New Haven, Connecticut 06520, USA*
[3]*Department of Mathematical Sciences, New Jersey Institute of Technology, Newark, New Jersey 07102, USA*

We study experimentally and computationally the dynamics of granular flow during impacts where intruders strike a collection of disks from above. In the regime where granular force dynamics are much more rapid than the intruder motion, we find that the particle flow near the intruder is proportional to the instantaneous intruder speed; it is essentially constant when normalized by that speed. The granular flow is nearly divergence free and remains in balance with the intruder, despite the latter's rapid deceleration. Simulations indicate that this observation is insensitive to grain properties, which can be explained by the separation of time scales between intergrain force dynamics and intruder dynamics. Assuming there is a comparable separation of time scales, we expect that our results are applicable to a broad class of dynamic or transient granular flows. Our results suggest that descriptions of static-in-time granular flows might be extended or modified to describe these dynamic flows. Additionally, we find that accurate grain-grain interactions are not necessary to correctly capture the granular flow in this regime.

What is the nature of force transmission and particle flow during dynamic intrusion into granular material? This question is fundamental to a general understanding of dense granular flow, and a complete description would have many applications, such as biological or robotic locomotions over sand [1,2] or impact into the surface of extraterrestrial bodies [3]. Moreover, the flow of grains during intrusion is part of a broad class of dense granular flows that are both rapid (i.e., large inertial number [4]) and highly transient in time. The highly transient driving seemingly prohibits the use of existing descriptions of dense granular flows [4–6], which are formulated for well developed cases (i.e., static in time after transients have settled or quasistatic). Additionally, the high speeds and accelerations involved in this process raise important questions on how these flows should be considered computationally, either with a discrete element method [7–9] or from a continuum perspective [10].

In this Rapid Communication, we present experimental and computational results on the flow of a two-dimensional granular material around circular intruders that are incident on a free granular bed at speeds of $v_0 \leqslant 6$ m/s. The main result from both experiments and simulations is that the flow of the granular material remains in a dynamic steady state with the intruder for essentially the entire trajectory, despite the highly transient nature of this process. By dynamic steady state, we mean that the granular flow field near the intruder scales linearly with the instantaneous intruder speed, even as the intruder decelerates rapidly. Since the force propagation speeds of $v_f \sim 300$ m/s $\gg v_0$ [11] are much faster than the intruder motion, forces can propagate and relax fast enough that the motion of grains near the intruder is essentially incompressible and remains in this dynamic steady state. We expect our results to be applicable to a wide array of rapid highly transient dense granular flows assuming $v_f \gg v_0$ (where v_0 sets a generic driving rate). Existing descriptions of well developed granular flows [4–6] may be extended or modified [10] to capture these transient flows. Additionally, whereas force propagation depends crucially on the intergrain

force law [11], the agreement between flow field measurements in simulations and experiments is largely independent of the grain properties used in the simulations, suggesting that accurate grain-grain interactions are not necessary to model highly dynamic flows, provided that $v_f \gg v_0$.

The experiments are carried out using the protocol described in Refs. [11–14]. Here, bronze intruders that are disks or have circular leading edges are normally incident from above on photoelastic disks. We measure the granular flow fields using particle image velocimetry (PIV) [15], which analyzes successive pairs of frames from high-speed movies (sampled at 2333 Hz) to estimate the local flow field. This returns estimates of the local displacement on a grid as shown in Fig. 1(a). The photoelastic disks are cut from PSM-1, manufactured by Vishay Precision Group. Here, $v_f \gg v_0$ [11], and we note that the grain-scale force picture and the subsequent intruder dynamics change drastically when $v_f \sim v_0$ [9,11]. However, when $v_f \gg v_0$, the intruder deceleration is dominated by large fluctuations in space and time in the form of quasirandom collisions with networks of particles that occur beneath the intruder [12,14]. Thus, our primary focus in this Rapid Communication is on the region directly beneath the intruder. The material responds quickly to the advancing intruder, and the fast force dynamics average over longer times to yield both rate-independent and Bagnold-like [16] velocity-squared drag forces that are common in both impact studies [12–14,17–21] (i.e., transient driving) and steady drag experiments [22–28] (i.e., well-developed flows). We note that our results help explain similarities between these two processes.

To explore the influence of the interaction force between the granular particles, we carried out simulations using both linear and nonlinear (Hertzian) force models that included friction as well as simulations with a linear force model and no interparticle friction. Simulations, described briefly below, are similar to those discussed in Ref. [9] but with a nonlinear force interaction model as well as parameters that are matched to the experiments. We consider a rectangular
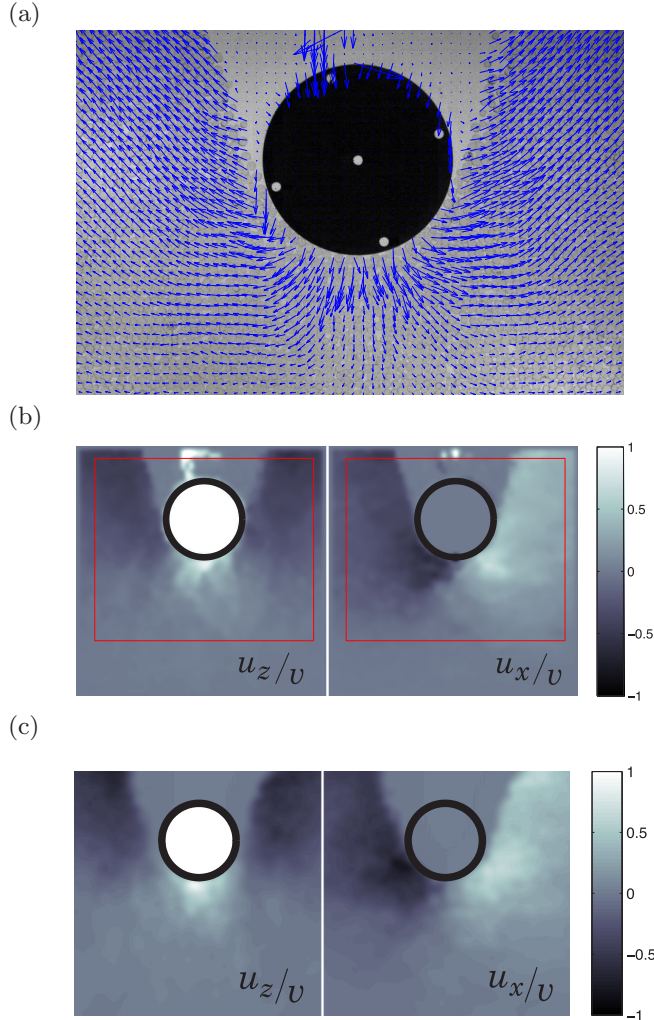
(a)

(b)

(c)

FIG. 1. (a) PIV flow field for a circular intruder with a radius of $R = 6.35$ cm at a particular frame. (b) Vertical and horizontal components of the spatially smoothed PIV flow field from experiment, normalized by the instantaneous intruder velocity ($v = 3.05$ m/s). The left panel shows the normalized vertical velocity u_z/v with downward as positive, and the right panel shows the horizontal velocity u_x/v with rightward as positive. The white color in the intruder in the left panel denotes its downward motion. The red box encloses the region used to obtain the steady-state velocity field, which will move along with the intruder. (c) The instantaneous flow fields u_z/v and u_x/v at a particular time from simulations with Hertzian frictional interactions between grains.

domain in two dimensions with gravity. The domain size as well as particle numbers and sizes are as in the experiments. The particle-particle, particle-intruder, and particle-wall interactions are modeled using the soft-sphere approach that includes friction and particle rotations. We then solve the following (nondimensional) equations of motion for each particle (including the intruder):

$$m_i \frac{d^2\mathbf{r}_i}{dt^2} = \mathbf{F}_{\mathrm{l}\,i,j}^n + \mathbf{F}_{\mathrm{l}\,i,j}^t + m_i\mathbf{g}, \quad I_i \frac{d\boldsymbol{\omega}_i}{dt} = -\frac{1}{2}d_i\mathbf{n} \times \mathbf{F}_{\mathrm{l}\,i,j}^t.$$

(1)

For the linear force model, the normal force is given by $\mathbf{F}_{\mathrm{l}\,i,j}^n = [k_n x - \gamma_n \bar{m}\mathbf{v}_{i,j}]\mathbf{n}$, where $r_{i,j} = |\mathbf{r}_{i,j}|$, $\mathbf{r}_{i,j} = \mathbf{r}_i - \mathbf{r}_j$, and the normal direction is defined by $\mathbf{n} = \mathbf{r}_{i,j}/r_{i,j}$. The compression is defined by $x = d_{\mathrm{ave}} - r_{i,j}$, where $d_{\mathrm{ave}} = (d_i + d_j)/2$, d_i and d_j are the diameters of the particles i and j, and $\mathbf{v}_{i,j}^n$ is the relative normal velocity.

The nondimensional force constant k_n is related to the dimensional one k by $k = k_n mg/d$, where m is the average particle mass, d is the average particle diameter, and g is Earth's gravity. All quantities are expressed using d as the length scale, the binary collision time $\tau_c = \pi\sqrt{d/2gk_n}$ as the time scale, and m as the mass scale. Then, $\bar{m}$ is the reduced mass, and γ_n is the damping coefficient related to the coefficient of restitution e_n by $\gamma_n = -2 \ln e_n/\tau_c$, see, e.g., Ref. [29]. We take $e_n = 0.5$ as a constant and ignore its possible velocity dependence [30]. The Hertzian interaction model is implemented as $\mathbf{F}_h = \sqrt{d_i d_j/(d_i + d_j)}\sqrt{x}\mathbf{F}_l$. In principle, the force constant could now be connected to the material properties of the particles using the method described, e.g., in Ref. [29]. Instead, here we use the results of static tests carried out to measure directly the functional relation between the normal force and the compression, see Ref. [11]. The normal force constant is then found using the measured value of the force for 1% compression. The tangential force is computed using a standard Cundall-Strack model [7]; see, e.g., Ref. [9] for the details of implementation. The particle-particle and particle-intruder coefficients of friction are set to the experimentally estimated value of $\mu = 0.8$ [31]; the particles making up the walls are made very inelastic and frictional with $\mu = 0.9$ and $e_n = 0.1$. The system is prepared by placing granular particles on a rectangular lattice with random size distribution of the particles. The particles are given random initial velocities and left to settle under gravity. Then, the whole domain is vibrated gently to let the particles settle once more. The intensity of vibrations does not appear to be important; we use $\Gamma = a\omega^2/g$ (a is the amplitude, and ω is the frequency of vibrations) in the range [1,5] without any systematic change in the results. We then place a circular intruder just above the bed with an initial downward velocity v_0.

Results from PIV (for experiments) or actual particle positions and velocities (for simulations) can be spatially coarse grained [32–34] as shown in Figs. 1(b) and 1(c) to give a continuum flow field $\mathbf{u}(\mathbf{x},t)$, where $\mathbf{x}$ represents spatial coordinates in the laboratory frame. The vertical component $u_z(\mathbf{x},t)$ (with downward being positive z) and the horizontal component $u_x(\mathbf{x},t)$ (with rightward being positive x) components of the flow field at an intruder speed of $v = 3.05$ m/s are shown in Fig. 1(b) for experiments. The grid size used for the PIV algorithm is approximately the same size as a single particle, so the particle-scale fluctuations in the velocity fields still persist. To compare simulation results to PIV, we use a coarse-grained momentum field normalized by the average mass density. (We normalize by the average mass density instead of a local mass density field since the coarse-grained spatially varying mass density field goes to zero at the free surface and near the intruder.) This yields a flow field $\mathbf{u}(\mathbf{r},t)/v$ as shown in Fig. 1(c) from simulations for an intruder radius of $R = 6.35$ cm.
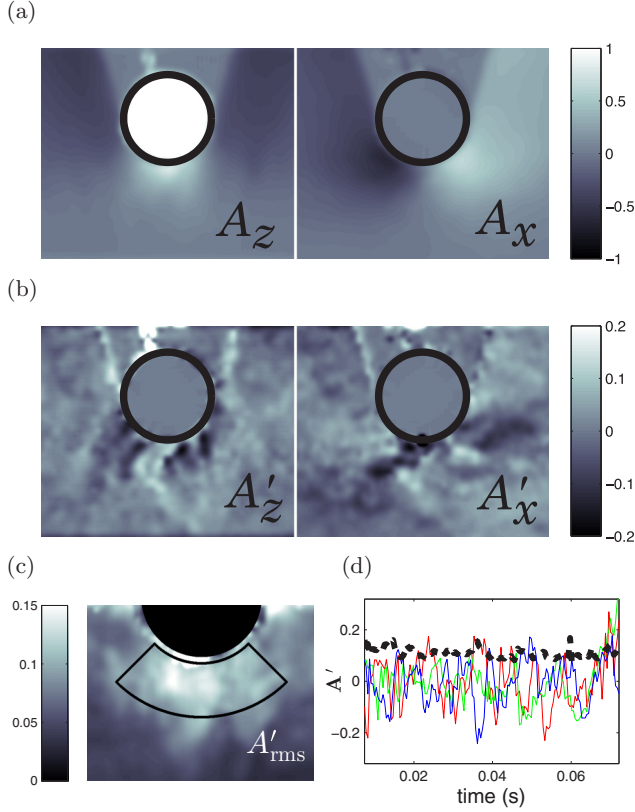
(a)

(b)

(c)   (d)

FIG. 2. (a) The average flow field **A** from experiments for a circular intruder with a radius of $R = 6.35$ cm. The left side shows the vertical velocity A_z (down is positive), and the right side shows the horizontal velocity A_x (right is positive). (b) The instantaneous fluctuations A'_z and A'_x in the flow field at a particular frame from experiments for a circular intruder with a radius of $R = 6.35$ cm. (c) A spatial plot of $A'_{\rm rms}$, the root-mean-squared value of **A'**. A time series of the spatial mean of $A'_{\rm rms}$ within the outlined region (where the fluctuations are most prominent) is plotted (thick dashed line) in panel (d). This quantity is essentially constant in time. The red, blue, and green solid lines in (d) show A'_z at three points beneath the intruder. These signals fluctuate around zero with a correlation time of roughly 3 ms.

In both experiments and simulations, we find that

$$\mathbf{u}(\mathbf{x},t) = v(t)[\mathbf{A}(\mathbf{x} - \mathbf{x}_0) + \mathbf{A}'(\mathbf{x} - \mathbf{x}_0,t)], \qquad (2)$$

where $v(t)$ is the intruder speed (with motion assumed to be strictly downward), $\mathbf{x}_0(t)$ is the intruder position in the laboratory frame, **A** is the scaled steady-state velocity field, and **A'** captures the instantaneous fluctuations in the velocity field. **A** and **A'** are shown in Figs. 2(a) and 2(b), respectively, for experiments. Similar fields for simulations with grain properties matched to those from the experiments (not shown) are indistinguishable by eye, and we quantitatively show that the two approaches agree in our analysis below. In each trajectory (experiments and simulations), we calculate **A** by time averaging the flow-field data inside the red rectangular region marked in Fig. 1(b). **A** appears very similar to the instantaneous flow fields shown in Figs. 1(b) and 1(c) but smoother spatially. **A'** is determined at each time from the difference between the instantaneous coarse-grained flow field

and the normalized space- and time-averaged flow field: $\mathbf{A}' = \mathbf{u}/v(t) - \mathbf{A}$. An experimental measurement of **A'** at one instant is shown in Fig. 2(b), which is typical for all times in both simulation and experiment.

We find the fluctuations **A'** to be strongest beneath the intruder, statistically stationary in time, and decoupled from the intruder dynamics. Figure 2(c) shows a spatial plot of the root-mean-square (rms) magnitude of the fluctuations $A'_{\rm rms}$. In the region beneath the intruder, the average fluctuations are about $|\mathbf{A}'| \approx 0.1$. The magnitude $|\mathbf{A}'|$ is always less than 0.2 (where a value of 1 would correspond to a local velocity fluctuation of the same size as the intruder speed); it is largest near the leading edge of the intruder and falls off rapidly with increasing distance from the intruder. Figure 2(d) shows time-series plots of **A'**, which are statistically stationary in time.

By analyzing local strain rates, we find that **A** represents a shear flow with zero divergence. Using numerical derivatives, we compute the strain-rate tensor for the average flow field $\mathbf{D} = 0.5[\nabla \mathbf{A} + (\nabla \mathbf{A})^\top]$ with eigenvalues d_1 and d_2. Figure 3 shows the local shear rate $\dot{\gamma}/v = (d_1 - d_2)/2$ and demonstrates that $\nabla \cdot \mathbf{A} = \mathrm{tr}\,\mathbf{D} = 0$ within noise, i.e., the flow of grains near the intruder is essentially incompressible. Note that $\dot{\gamma}/v$ is well correlated to $A'_{\rm rms}(\mathbf{r})$, shown in Fig. 2(c). This is similar to many previous studies [35,36] where shear causes local velocity fluctuations. Physically, **A'** represents nonaffine particle rearrangements as particles are forced to move past each other as opposed to a monotonic increase or decrease as the intruder slows. A full analysis of grain-scale fluctuations, which could be achieved with data for particle trajectories (as opposed to PIV), will be a topic of future work.

Combined with force data from previous studies [12–14], the strain rates shown in Fig. 3 can be used to estimate the inertial number $I = \dot{\gamma}\sqrt{m/P}$, which is often used to determine a constitutive relation for granular shear flows [4–6]. Here, m is mass of a single grain, and P is the local pressure. The maximum shear rate in Fig. 3 is $\dot{\gamma} \approx 20v$, and the mass of a grain m is roughly 0.1 g. We estimate the pressure $P \sim F/D$ by considering the force F on the intruder and dividing by the intruder diameter D. F is dominated by velocity-squared forces which arise from collisions with force-chain-like structures [14], and for circular intruders in the present experiments, we find $F \approx h_0 v^2$, where h_0 is a shape and size dependent constant with units of kg/m; for the circular-nosed intruders considered here, we find $h_0/D \approx 5$ kg/m^2 [14]. This yields $I \approx 0.09$ in the region directly beneath the

FIG. 3. The local shear rate $\dot{\gamma}/v$ and the divergence of **A**, computed numerically from the flow field shown in Fig. 2(a), showing that **A** is a divergence-free shear flow.

intruder, which is in the rapid flow regime where nonlocal effects may be less important [6,37].

To quantitatively compare $\mathbf{A}$ for various intruder sizes and simulation settings, we fit $\mathbf{A}$ to a functional form by decomposing it into radial and angular components,

$$\mathbf{A}(\mathbf{x}) = \hat{\mathbf{r}}[\cos\theta - f_r(\mathbf{r})] + \hat{\boldsymbol{\theta}}[f_\theta(\mathbf{r}) - \sin\theta]. \quad (3)$$

Here, $\mathbf{r} = r\hat{\mathbf{r}} + \theta\hat{\boldsymbol{\theta}}$, where $\mathbf{r} = 0$ corresponds to the center of the intruder and θ is measured counterclockwise from the (downward) z axis. The components f_r and f_θ represent the flow field components in the intruder frame, and shifting by $\hat{\mathbf{z}} = \cos\theta\hat{\mathbf{r}} - \sin\theta\hat{\boldsymbol{\theta}}$ transfers these components back to the laboratory frame, where $\mathbf{A}$ is defined. f_r and f_θ are defined as

$$f_r(\mathbf{r}) = a_r(r)\cos[b_r(r)\theta], \quad (4)$$

$$f_\theta(\mathbf{r}) = a_\theta(r)\sin[b_\theta(r)\theta]. \quad (5)$$

(a)

(b)   (c)
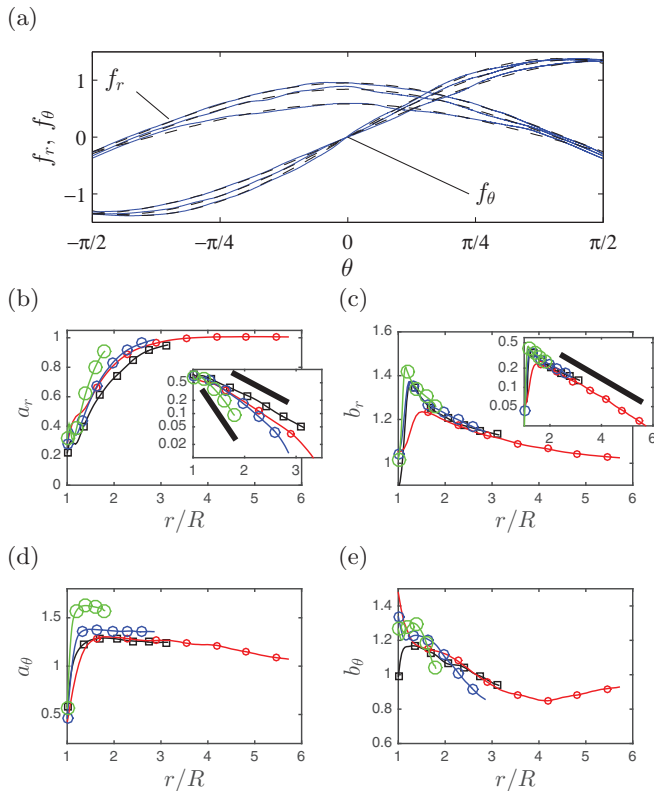
(d)   (e)

FIG. 4. (a) Data (solid blue lines) and corresponding fit line (dashed black lines) of the form shown in Eq. (3) for one intruder (radius of $R = 3.18$ cm) at $r = 1.5R$, $2R$, and $3R$, where $r = R$ corresponds to the intruder boundary. (b)–(e) A comparison of the fit parameters—$a_r(r), b_r(r), a_\theta(r), b_\theta(r)$—for circular intruders with $R = 3.18$ cm (small red circles) $R = 6.35$ cm (medium blue circles), $R = 10.15$ cm (large green circles), as well as the circular-nosed intruder with $R = 4.65$ cm and a rectangular tail (black squares). The inset of (b) shows semilogarithmic plots of $1 - a_r(r)$ versus r/R; the thick black reference lines show exponential decay with decay lengths of $0.7R$ (upper) and $0.25R$ (lower). The inset of (c) shows semilogarithmic plots of $b_r(r) - 1$ versus r/R; the thick black reference line shows exponential decay with a decay length of $1.85R$.

Seguin and co-workers [25,26] used a similar form to describe quasistatic granular flow around downward-moving circular obstacles but with $b_r = b_\theta = 1$ since in their quasistatic case, the flow was symmetric ahead of and behind the intruder. Here, we consider fits only to the half-space in front of the intruder. Sample fits at particular values of r are shown in Fig. 4. Far away, all four fit parameters should approach 1, corresponding to no grain motion.

Figure 4 shows $a_r(r)$, $b_r(r)$, $a_\theta(r)$, and $b_\theta(r)$ for different circular-nosed intruders with radii of $R = 3.18, 4.65, 6.35$, and 10.15 cm. The intruder with $R = 4.65$ cm is an ogive, with a circular nose and rectangular tail; however, the particles are never in contact with the tail so that its presence is irrelevant, aside from increasing the area of the intruder and therefore its mass. The fit parameters for each intruder appear similar when rescaled by R with secondary dependencies on the ratio ρ_{int}/ρ_g of the intruder to grain mass density and on the ratio d/R of grain size to intruder radius, where $d \approx 5$ mm. a_r and b_r decay roughly exponentially to their far-field values as $a_r \propto \exp(-r/\xi_{a_r})$ and $b_r \propto \exp(-r/\xi_{b_r})$ with $0.25R < \xi_{a_r} < 0.7R$ and $\xi_{b_r} \approx 1.85R$. This localization and exponential spatial decay is also common in dense granular flows that are driven by a boundary (e.g., Refs. [25,26,36] and many others).

Figure 5 shows a comparison between the fit of experimental and computational data to Eqs. (3)–(5) for a single size intruder; this is typical for all sizes. We find surprisingly good agreement for all considered interparticle force models (frictional Hertzian, frictional linear, and frictionless linear interactions). Such good agreement shows that in the present regime where $v_0 \ll v_f$, the details of the force model are not
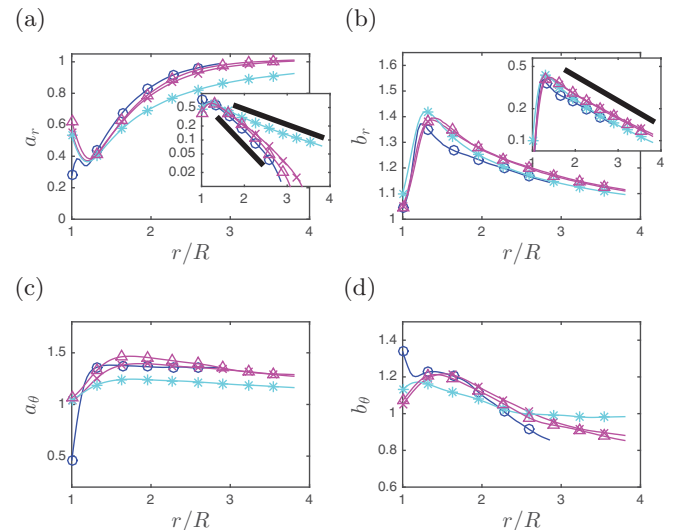

(a)   (b)

(c)   (d)

FIG. 5. Comparison of the parameters $a_r(r)$, $b_r(r)$, $a_r(r)$, and $a_\theta(r)$ between experimental data (blue circles) from Fig. 4 and simulations using frictional linear (magenta crosses), frictional Hertzian (magenta triangles), and frictionless linear (light blue asterisks) interactions, all under the same conditions with $R = 6.35$ cm. The insets of (a) and (b) show semilogarithmic plots of $1 - a_r(r)$ and $b_r(r) - 1$, respectively, versus r/R. The thick black reference lines in the insets show exponential decay with decay lengths of (a) of $1.3R$ (upper) and $0.45R$ (lower) and in (b) of $1.85R$.

crucial for the response of granular material. However, we note that frictional forces primarily affect the decay length of the radial flow field as shown in the inset of Fig. 5(a), and thus they play an important role in determining dynamics of the intruder; in particular, without friction, the final penetration depth is almost 50% larger (roughly 60 cm) than when friction is present (roughly 42 cm). The functional form of the normal forces between the particles (linear versus nonlinear) however does not appear to be important.

These results provide several important physical insights that should be applicable to a broad class of shearlike flows that are both rapid and highly transient but where driving speed, which is here set by $v(t) \leqslant v_0$, is still very slow compared to the granular force transmission speed v_f. In the granular flow fields, we observe none of the elasticlike response (i.e., loading and unloading) that is dominant when $v_0 \sim v_f$ [9,11]. Instead, we observe that the particle motion scales linearly with driving speed, which also occurs for well-developed shear flows in the limits of both small (quasistatic) and large (rapid driving) inertial number I with a transition region in between [6,38]. Our system is clearly more akin to the limit of large I with $I \sim 10^{-1}$ at the leading edge of the intruder, but descriptions of such flows explicitly exclude transients in the driving speed. However, we observe a dynamic steady state of the granular flow during highly transient driving, which suggests that rapid highly transient granular flows may fall into the same class as well-developed rapid flows, provided $v_f \gg v_0$. Conversely, it is possible that models, such as $\mu(I)$ could be extended to processes, such as granular impact where the flow is transient. For example, a recent study [10] presents a modified $\mu(I)$ rheology to study dynamic granular flows, and our results here suggest that this approach will likely be successful in many cases. In addition, simulations show that, although final penetration depth is strongly influenced by frictional interactions, the granular flow in this regime appears relatively insensitive to the form of the grain-grain force law (e.g., linear versus Hertzian, consistent with Ref. [39]) or even to the presence of friction [14,40].

[1] C. Li, T. Zhang, and D. I. Goldman, A terradynamics of legged locomotion on granular media, Science **339**, 1408 (2013).

[2] J. Aguilar and D. I. Goldman, Robophysical study of jumping dynamics on granular media, Nat. Phys. **12**, 278 (2016).

[3] S. R. Schwartz, P. Michel, D. C. Richardson, and H. Yano, Low-speed impact simulations into regolith in support of asteroid sampling mechanism design I: Comparison with 1-g experiments, Planet. Space Sci. **103**, 174 (2014).

[4] F. da Cruz, S. Emam, M. Prochnow, J.-N. Roux, and F. Chevoir, Rheophysics of dense granular materials: Discrete simulation of plane shear flows, Phys. Rev. E **72**, 021309 (2005).

[5] P. Jop, Y. Forterre, and O. Pouliquen, A constitutive law for dense granular flows, Nature (London) **441**, 727 (2006).

[6] K. Kamrin and G. Koval, Nonlocal Constitutive Relation for Steady Granular Flow, Phys. Rev. Lett. **108**, 178301 (2012).

[7] P. A. Cundall and O. D. L. Strack, A discrete numerical model for granular assemblies, Géotechnique **29**, 47 (1979).

[8] M. Pica Ciamarra, A. H. Lara, A. T. Lee, D. I. Goldman, I. Vishik, and H. L. Swinney, Dynamics of Drag and Force Distributions for Projectile Impact in a Granular Medium, Phys. Rev. Lett. **92**, 194301 (2004).

[9] L. Kondic, X. Fang, W. Losert, C. S. O'Hern, and R. P. Behringer, Microstructure evolution during impact on granular matter, Phys. Rev. E **85**, 011305 (2012).

[10] S. Dunatunga and K. Kamrin, Continuum modeling and simulation of granular flows through their many phases, J. Fluid Mech. **779**, 483 (2015).

[11] A. H. Clark, A. J. Petersen, L. Kondic, and R. P. Behringer, Nonlinear Force Propagation During Granular Impact, Phys. Rev. Lett. **114**, 144502 (2015).

[12] A. H. Clark, L. Kondic, and R. P. Behringer, Particle Scale Dynamics in Granular Impact, Phys. Rev. Lett. **109**, 238302 (2012).

[13] A. H. Clark and R. P. Behringer, Granular impact model as an energy-depth relation, Europhys. Lett. **101**, 64001 (2013).

[14] A. H. Clark, A. J. Petersen, and R. P. Behringer, Collisional model for granular impact dynamics, Phys. Rev. E **89**, 012201 (2014).

[15] I Grant, Particle image velocimetry: A review, Proc. Inst. Mech. Eng., Part C **211**, 55 (1997).

[16] R. A. Bagnold, Experiments on a gravity-free dispersion of large solid spheres in a newtonian fluid under shear, Proc. R. Soc. London, Ser. A **225**, 49 (1954).

[17] W. A. Allen, E. B. Mayfield, and H. L. Morrison, Dynamics of a projectile penetrating sand, J. Appl. Phys. **28**, 370 (1957).

[18] M. J. Forrestal and V. K. Luk, Penetration into soil targets, Int. J. Impact Eng. **12**, 427 (1992).

[19] H. Katsuragi and D. J. Durian, Unified force law for granular impact cratering, Nat. Phys. **3**, 420 (2007).

[20] D. I. Goldman and P. Umbanhowar, Scaling and dynamics of sphere and disk impact into granular media, Phys. Rev. E **77**, 021308 (2008).

[21] P. Umbanhowar and D. I. Goldman, Granular impact and the critical packing state, Phys. Rev. E **82**, 010301 (2010).

[22] R. Albert, M. A. Pfeifer, A.-L. Barabási, and P. Schiffer, Slow Drag in a Granular Medium, Phys. Rev. Lett. **82**, 205 (1999).

[23] I. Albert, J. G. Sample, A. J. Morss, S. Rajagopalan, A.-L. Barabási, and P. Schiffer, Granular drag on a discrete object: Shape effects on jamming, Phys. Rev. E **64**, 061303 (2001).

[24] J. Geng and R. P. Behringer, Slow drag in two-dimensional granular media, Phys. Rev. E **71**, 011302 (2005).

[25] A. Seguin, Y. Bertho, P. Gondret, and J. Crassous, Dense Granular Flow Around a Penetrating Object: Experiment and Hydrodynamic Model, Phys. Rev. Lett. **107**, 048001 (2011).

[26] A. Seguin, Y. Bertho, F. Martinez, J. Crassous, and P. Gondret, Experimental velocity fields and forces for a cylinder penetrating into a granular medium, Phys. Rev. E **87**, 012201 (2013).

[27] Y. Takehara, S. Fujimoto, and K. Okumura, High-velocity drag friction in dense granular media, Europhys. Lett. **92**, 44003 (2010).

[28] Y. Takehara and K. Okumura, High-Velocity Drag Friction in Granular Media Near the Jamming Point, Phys. Rev. Lett. **112**, 148001 (2014).

[29] L. Kondic, Dynamics of spherical particles on a surface: Collision-induced sliding and other effects, Phys. Rev. E **60**, 751 (1999).

[30] J. Schäfer, S. Dippel, and D. E. Wolf, Force schemes in simulations of granular materials, J. Phys. I France **6**, 5 (1996).

[31] J. G. Puckett and K. E. Daniels, Equilibrating Temperaturelike Variables in Jammed Granular Subsystems, Phys. Rev. Lett. **110**, 058001 (2013).

[32] I. Goldhirsch and C. Goldenberg, On the microscopic foundations of elasticity, Eur. Phys. J. E **9**, 245 (2002).

[33] I. Goldhirsch, Stress, stress asymmetry and couple stress: from discrete particles to continuous fields, Granular Matter **12**, 239 (2010).

[34] A. H. Clark, P. Mort, and R. P. Behringer, Coarse graining for an impeller-driven mixer system, Granular Matter **14**, 283 (2012).

[35] N. Menon and D. J. Durian, Diffusing-wave spectroscopy of dynamics in a three-dimensional granular flow, Science **275**, 1920 (1997).

[36] W. Losert, L. Bocquet, T. C. Lubensky, and J. P. Gollub, Particle Dynamics in Sheared Granular Matter, Phys. Rev. Lett. **85**, 1428 (2000).

[37] D. L. Henann and K. Kamrin, A predictive, size-dependent continuum model for dense granular flows, Proc. Natl. Acad. Sci. USA **110**, 6730 (2013).

[38] G. Koval, J.-N. Roux, A. Corfdir, and F. Chevoir, Annular shear of cohesionless granular materials: From the inertial to quasistatic regime, Phys. Rev. E **79**, 021306 (2009).

[39] C. S. Campbell, Granular shear flows at the elastic limit, J. Fluid Mech. **465**, 261 (2002).

[40] A. Seguin, Y. Bertho, P. Gondret, and J. Crassous, Sphere penetration by impact in a granular medium: A collisional process, Europhys. Lett. **88**, 44002 (2009).